

SCIENTIFIC REPORTS

OPEN

Epitaxial thin films of pyrochlore iridate $\text{Bi}_{2+x}\text{Ir}_{2-y}\text{O}_{7-\delta}$: structure, defects and transport properties

W. C. Yang¹, Y. T. Xie², W. K. Zhu¹, K. Park², A. P. Chen³, Y. Losovyj⁴, Z. Li^{1,3}, H. M. Liu¹, M. Starr¹, J. A. Acosta¹, C. G. Tao², N. Li³, Q. X. Jia^{3,5}, J. J. Heremans² & S. X. Zhang¹

While pyrochlore iridate thin films are theoretically predicted to possess a variety of emergent topological properties, experimental verification of these predictions can be obstructed by the challenge in thin film growth. Here we report on the pulsed laser deposition and characterization of thin films of a representative pyrochlore compound $\text{Bi}_2\text{Ir}_2\text{O}_7$. The films were epitaxially grown on yttria-stabilized zirconia substrates and have lattice constants that are a few percent larger than that of the bulk single crystals. The film composition shows a strong dependence on the oxygen partial pressure. Density-functional-theory calculations indicate the existence of Bi_i antisite defects, qualitatively consistent with the high Bi: Ir ratio found in the films. Both Ir and Bi have oxidation states that are lower than their nominal values, suggesting the existence of oxygen deficiency. The iridate thin films show a variety of intriguing transport characteristics, including multiple charge carriers, logarithmic dependence of resistance on temperature, antilocalization corrections to conductance due to spin-orbit interactions, and linear positive magnetoresistance.

Iridates have recently emerged as a fertile ground for novel topological electronic states that arise from the interplay of electron interactions and spin-orbit coupling^{1–9}. In particular, the pyrochlore compounds with a chemical formula of $\text{A}_2\text{Ir}_2\text{O}_7$ (A-227, where A = Bi, Y or rare-earth element) are predicted to host a variety of topological phases, including topological Mott insulators^{3, 4}, Weyl semimetals⁶, topological crystalline insulators¹⁰, and Weyl-Mott insulators¹¹. The pyrochlore iridate compounds have a cubic crystal structure ($Fm\bar{3}m$), in which the A^{3+} and Ir^{4+} cations form inter-penetrating networks of corner-sharing tetrahedra. The energy scale of electron interaction relative to electron hopping (i.e. U/t) increases monotonically as the A-site ionic radius decreases¹²; and the electrical transport properties can be divided roughly into three categories^{8, 13}: 1) compounds with large A^{3+} (e.g. Bi-227 and Pr-227) show a metallic behavior down to the lowest measured temperature T ^{5, 13–16}; 2) those with intermediate A^{3+} (e.g. Eu-227 and Nd-227) display a metal-to-insulator transition^{13, 16–19}, which is often accompanied by a paramagnetic to an antiferromagnetic phase transition; and 3) substances with small A^{3+} (e.g. Lu-227 and Yb-227) exhibit an insulating-like behavior^{13, 15, 20} throughout the entire region of T .

While significant experimental progress has recently been made in bulk A-227 compounds^{5, 17–38}, including the demonstration of all-in/all-out non-collinear magnetic order^{24, 38}, observation of giant magnetoresistance associated with metallic domain walls^{34–36} and indication of Weyl semimetal phases^{18, 37}, there are only a few studies on thin film samples^{39–43}, which is largely due to the great challenges in obtaining high quality films. Theoretical studies on pyrochlore iridate thin films have suggested a variety of emergent topological properties, including the quantized anomalous Hall conductance⁴⁴ and the correlated Chern insulator⁴⁵ that are otherwise not accessible in bulk samples. While these topological properties have yet been realized experimentally, remarkable transport phenomena have been observed in thin films, including a linear magnetoresistance (MR) up to 35 Tesla in Bi-227³⁹ and a cooling field-dependent, asymmetric MR in Eu-227⁴⁰. Moreover, thin film structures provide an excellent platform to engineer physical properties by means of, for example, electric gating and elastic strain, offering great potentials for device applications.

¹Department of Physics, Indiana University, Bloomington, Indiana, 47405, USA. ²Department of Physics, Virginia Tech, Blacksburg, Virginia, 24061, USA. ³Center for Integrated Nanotechnologies, Los Alamos National Laboratory, Los Alamos, 87545, USA. ⁴Department of Chemistry, Indiana University, Bloomington, Indiana, 47405, USA. ⁵Department of Materials Design and Innovation, University at Buffalo, The State University of New York, Buffalo, NY, 14260, USA. W. C. Yang, Y. T. Xie and W. K. Zhu contributed equally to this work. Correspondence and requests for materials should be addressed to S.X.Z. (email: sxzhang@indiana.edu)

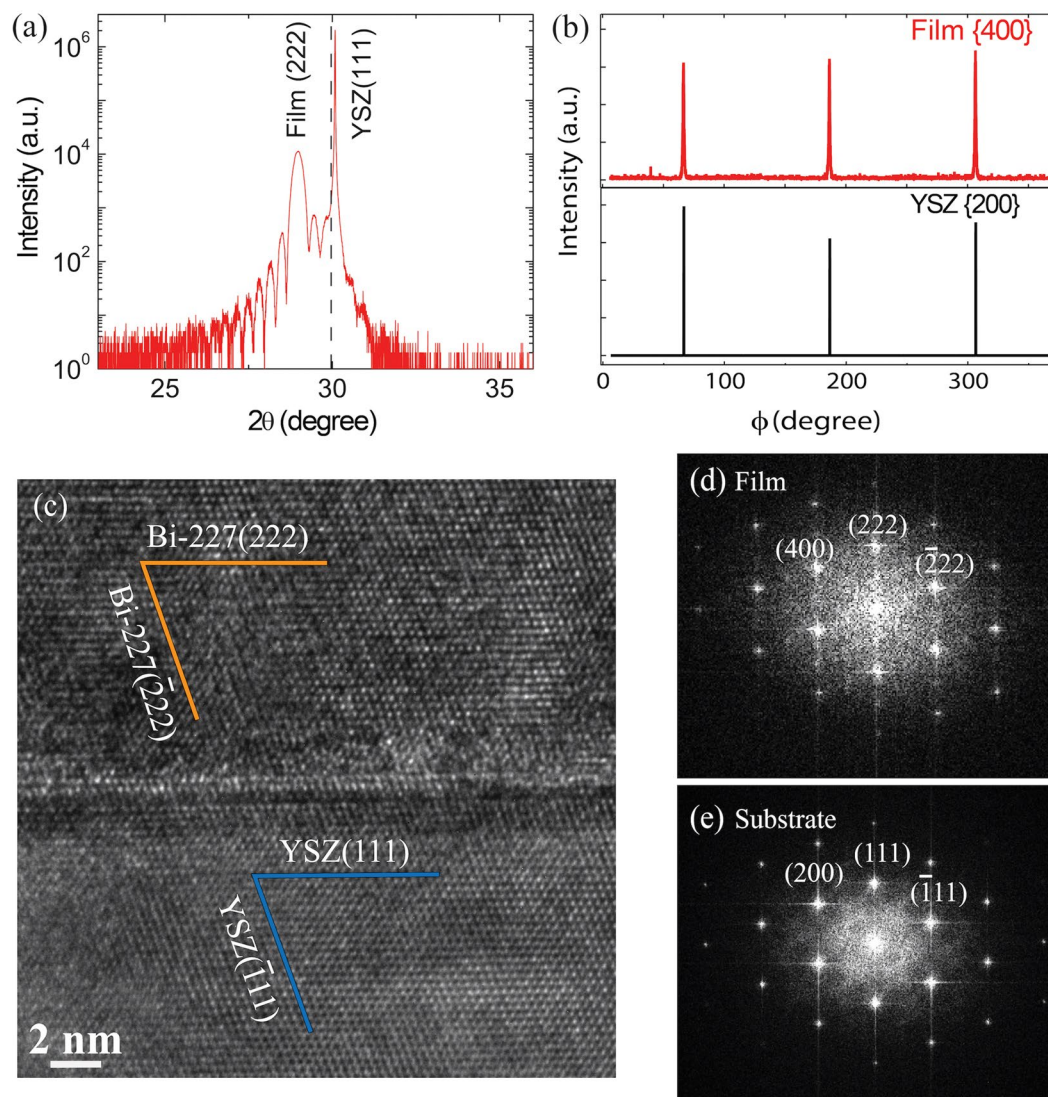


Figure 1. X-ray diffraction characterizations and TEM studies of a representative Bi-227 thin film grown at $P_{O_2} = 50$ mTorr using Ir/Bi@1 target (f1): (a) 2θ - ω scan around YSZ (111) reflection showing the (111) and (222) peaks of the substrate and thin film, respectively. The dashed line indicates the (222) peak position of the bulk single crystal Bi-227^{14,29}. (b) in-plane φ -scan for the {200} of YSZ substrate and the {400} of thin film. (c) Cross-sectional TEM image taken at the interface of thin film and substrate; Fast Fourier Transform images from (d) thin film and (e) substrate.

In this paper, we report on systematic measurements of the structural, compositional, and electrical transport properties of a prototypical pyrochlore iridate, namely Bi-227 thin films. The films were grown epitaxially along the [111] direction on the yttrium-stabilized zirconia (YSZ) (111) substrates by pulsed laser deposition (PLD). The out-of-plane lattice parameters of thin films were found to be a few percent larger than that of the bulk samples. Compositional characterizations, density-functional-theory (DFT) calculations, along with X-ray photoelectron spectroscopy (XPS) studies suggest the existence of Bi_{Ir} antisite defects and oxygen vacancies. With varied defect densities, thin films show a broad spectrum of electronic transport characteristics, including multiple charge carriers, logarithmic dependence of resistance on T , antilocalization, and linear positive magnetoresistance.

Results and Discussions

PLD growth, structural and compositional characterizations. Thin films were grown by PLD using two targets that were prepared via a solid state reaction method with IrO₂ and Bi₂O₃ as source materials at Ir/Bi ratios of 1 and 3 (labeled as Ir/Bi@1 target and Ir/Bi@3 target, respectively). X-ray diffraction (XRD) measurements suggest that thin films are epitaxially grown on the YSZ substrates along the [111] direction of a cubic phase. Figure 1(a) shows a local $2\theta - \omega$ scan taken on a representative film grown at oxygen partial pressure $P_{O_2} = 50$ mTorr using the Ir/Bi@1 target. A well-defined oscillation was observed near the thin film (222) peak, indicating a high crystalline quality and smooth film surface. The film thickness was determined to be ~ 26 nm

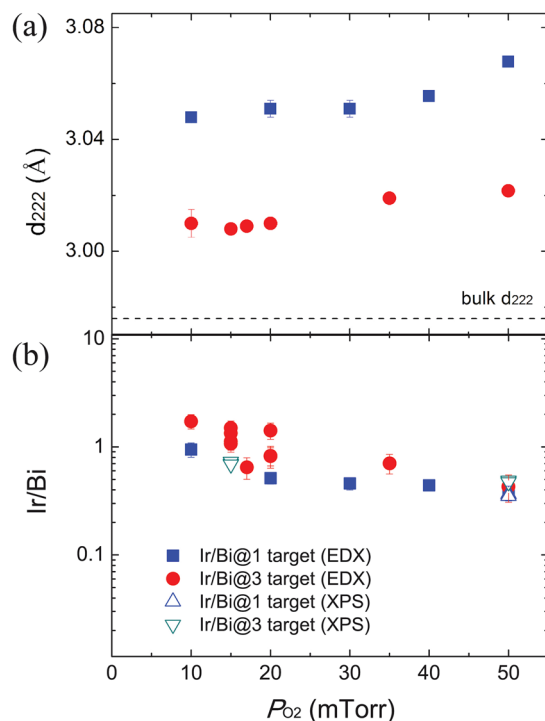


Figure 2. (a) lattice spacing d_{222} versus oxygen pressure P_{O_2} . The error bars were estimated according to the diffraction peaks. (b) Ir/Bi ratio versus P_{O_2} (multiple data points at the same pressure were taken at different spots/areas of the sample). The error bars were determined based on the EDX analysis in the AZtech software.

based on the X-ray reflectivity. The out-of-plane d -spacing for the (222) film peak (d_{222}) is ~ 3.07 Å, which is $\sim 3\%$ larger than that of bulk Bi-227, i.e., $d_{222} \sim 2.98$ Å^{14,29}. The in-plane φ -scan shows a clear three-fold symmetry (Fig. 1 (b)), confirming that the film has a cubic crystalline structure and is epitaxially grown on the substrate. The epitaxial relationship between the thin film and the substrate was determined to be (222)Bi-227||[111]YSZ and [02 $\bar{2}$]Bi-227||[01 $\bar{1}$]YSZ based on the φ -scan and the cross-sectional transmission electron microscopy (TEM) measurements (Fig. 1(c,d and e)).

We note that elongation (contraction) in the out-of-plane d -spacing was also observed in a layered iridate Sr_2IrO_4 and its origin was demonstrated to be in-plane compression (tension)^{46,47}. While a compressive in-plane strain may exist in the Bi-227 film due to its lattice mismatch with the substrate ($a_{\text{bulk Bi-227}} \sim 10.32$ Å versus $2a_{\text{YSZ}} \sim 10.25$ Å), the elongation in out-of-plane d -spacing here cannot be solely attributed to the in-plane compression. Indeed, a 1.5% in-plane compression is required for 3% out-of-plane elongation in order to maintain the unit cell volume constant. However, the lattice mismatch between the film (assuming bulk lattice constant) and the substrate is only 0.6%, smaller than the required compression. To understand the origin of the large lattice elongation, we further carried out film growth at different P_{O_2} using two different targets since oxygen content and cation stoichiometry can be strongly correlated with the out-of-plane lattice parameters in complex oxide thin films^{48–50}. As shown in Fig. 2(a), the spacing d_{222} (and hence the lattice constant $a = 2\sqrt{3}d_{222}$ of the cubic unit cell) decreases with the decrease of P_{O_2} . At the same P_{O_2} , the film grown using the Ir/Bi@3 target has a smaller lattice constant than that grown using the Ir/Bi@1 target. The minimum d_{222} (or a) obtained in these films is still $\sim 1.3\%$ larger than that of the bulk sample. To gain further insight, we characterized the chemical compositions of the films using two complementary techniques, i.e. XPS and energy-dispersion X-ray spectroscopy (EDX) which show consistent dependence of Ir/Bi ratio on P_{O_2} (Fig. 2(b)). The ratio increases from ~ 0.4 to ~ 1 when P_{O_2} is decreased from 50 mTorr to 10 mTorr. The low Ir/Bi ratio at high P_{O_2} should be attributed to the high vapor pressure of IrO_3 . We also note that a Pt/Bi ratio of ~ 0.62 (or Bi/Pt ~ 1.62) was determined in another pyrochlore film $Bi_2Pt_2O_7$ ⁵¹; these results suggest that the pyrochlore phase is stable over a wide range of compositions. When P_{O_2} is 30 mTorr or lower, a small Ir (111) peak is observed in the XRD pattern (see Supplementary Fig. S1), indicating the formation of Ir metal impurity. The film grown at $P_{O_2} = 1$ mTorr is dominated by Ir metal and the Ir/Bi ratio is found to be >10 (see Supplementary Figs S1 and S2(c)). The high Ir/Bi ratio obtained in low P_{O_2} may be attributed to the high volatility of Bi metal and stability of Ir. At the same P_{O_2} , the films deposited from the Ir/Bi@3 target have slightly higher Ir/Bi ratios than the ones from the Ir/Bi@1 target. Nevertheless, the dependence of film composition on the target is much weaker than on P_{O_2} .

Density Functional Theory Calculations. The low Ir/Bi ratio in the films grown at high P_{O_2} indicates the possible existence of antisite (Bi_{Ir}) and/or Bi interstitial (Bi_{int}) defects which can result in a larger lattice constant than the stoichiometric compound (the ionic radius of Bi^{3+} is larger than Ir^{4+}). To verify this possibility, we computed the formation energies of the above two types of defects via DFT calculations, in which a range of chemical

Bi: Ir antisite [Bi interstit.]	Case 1	Case 2	Case 3	Case 4	Case 5
$\Delta_{\text{Bi}}^{T=0}$ (eV)	0	-3.77	0	-2.20	0
$\Delta_{\text{Ir}}^{T=0}$ (eV)	-7.54	-3.77	-5.79	-2.20	0
$\Delta\mu_{\text{O}}^{T=0}$ (eV)	0	0	-0.5	-0.9	-2.15
Form. Eng. ΔE_f (eV)	-7.47 [4.86]	-4.04 [6.50]	-5.72 [4.86]	-4.04 [4.93]	4.04 [4.86]
Notes	ΔE_f at $T=550$ C, $P=50$ mTorr	ΔE_f at $T=550$ C, $P=15$ mTorr	ΔE_f at $T=550$ C, $P=50$ mTorr	ΔE_f at $T=550$ C, $P=15$ mTorr	ΔE_f at $T=0$

Table 1. Calculated formation energies ΔE_f of a single Bi_{Ir} defect and a Bi_{int} in the pyrochlore structure of $\text{Bi}_2\text{Ir}_2\text{O}_7$ with the chemical potential differences of Bi, Ir, and O, $\Delta_{\text{Bi}}^{T=0}$, $\Delta_{\text{Ir}}^{T=0}$, and $\Delta\mu_{\text{O}}^{T=0}$ at $T=0$ in five different cases. The un-bracketed (bracketed) numbers are the formation energies of the Bi_{Ir} (Bi_{int}) defect. Here the minimum value of both $\Delta_{\text{Bi}}^{T=0}$ and $\Delta_{\text{Ir}}^{T=0}$ is -7.54 eV, and the minimum value of $\Delta\mu_{\text{O}}^{T=0}$ is -2.15 eV, considering the zero-temperature DFT-calculated $\text{Bi}_2\text{Ir}_2\text{O}_7$ formation enthalpy per unit (consisting of 2 Bi, 2 Ir, and 7 O atoms) to be -15.08 eV. For the calculation of ΔE_f , the temperature and oxygen pressure dependence of $\Delta\mu_{\text{O}}$ was included except for Case 5.

potential differences of Bi, Ir and O are considered (Table 1). When the chemical potential of elemental Bi, Ir, or O is the same as that of bulk Bi, bulk Ir, or O_2 gas, respectively, i.e. the chemical potential difference is zero, the Bi, Ir, or O is said to be in an “abundant” condition. A decrease of chemical potential difference corresponds to the decrease of element content; in other words, the lower the chemical potential difference is, the “more deficient” the element is. Our calculations show that the Bi_{int} defects have a consistently high formation energy (4.86 ~6.50 eV), indicating a low possibility of this defect in the films. In contrast, the formation energy of the antisite Bi_{Ir} defect varies from negative to positive, depending mainly on the oxygen content or the chemical potential difference between the element O and O_2 gas. When oxygen is abundant (cases #1 and 2) or slightly deficient (cases #3 and 4), the formation energy is found to be negative. Comparing case #1 with #2 (or #3 with #4) suggests that the more deficient the Ir is, the more stable the Bi_{Ir} defect is; furthermore, comparison between cases #1 and 3 (or between #2 and 4) indicates that the more abundant the oxygen is, the more stable the defect is. Particularly, in case #1 when oxygen is abundant and Ir is deficient, the formation energy reaches a minimum value of -7.47 eV, suggesting that the antisite defect is very stable in this condition. The calculated result is qualitatively consistent with the experimental result in Fig. 2(a), i.e. the Ir/Bi ratio in the film increases as P_{O_2} decreases. When oxygen is very deficient but Bi and Ir are abundant (case #5), the antisite defect is unlikely to form as indicated by a positive formation energy of 4.04 eV, consistent with the high Ir/Bi (>10) observed at the lowest P_{O_2} (see Supplementary Fig. S2(c)).

X-ray photoelectron spectroscopy studies of oxidation states. The films grown at $P_{\text{O}_2} = 15\sim 50$ mTorr were found to be slightly oxygen-deficient, as suggested by the XPS studies. The XPS measurement was taken on three representative films, i.e. f1 ($P_{\text{O}_2} = 50$ mTorr, Ir/Bi@1 target), f2 ($P_{\text{O}_2} = 50$ mTorr, Ir/Bi@3 target), and f3 ($P_{\text{O}_2} = 15$ mTorr, Ir/Bi@3 target), along with two control samples, i.e. bulk IrO_2 and Bi_2O_3 . The Ir 4f spectrum and Bi 4f spectrum for films f1 and f3 are presented in Fig. 3, and the same for f2 are provided in the Supplementary Fig. S3. A qualitative comparison between the spectra of the films and that of the bulk IrO_2 (and Bi_2O_3) (see Supplementary Fig. S4) suggests that both Ir (and Bi) have a component with an oxidation state lower than the nominal +4 (and +3). We fitted the spectra using two components in CasaXPS software to obtain more quantitative information. The symmetric component is described by the Gaussian-Lorentz profile $\text{GL}(m)$, while the asymmetric lineshape which is used to capture the many-body, screening effects⁵² is described by the convolution of Gelius profile $\text{A}(a,b,n)$ and Gaussian-Lorentz profile $\text{GL}(m)$, in which the asymmetry is determined by the parameters a and b . More detailed information about the fitting process is provided in the supplemental information. The fitting spectra at the optimal a and b values are shown in Fig. 3. The obtained binding energies for Ir $4f_{5/2}$ peaks are: 65.8~66.1 eV (component 1) and 64.4~64.5 eV (component 2); the binding energies for Ir $4f_{7/2}$ peaks are: 62.8~63.1 eV (component 1); and 61.4~61.5 eV (component 2). The existence of two components may be attributed to the appearance of two final states in the photoemission process^{53, 54}, the coexistence of the core lines and plasmon satellite^{55, 56}, and a mixed oxidation state⁵⁷. In either case, however, the fact that the entire measured spectra are shifted to lower binding energies in comparison to IrO_2 (Ir^{4+}) suggests the formation of oxygen vacancies in the films. Similarly, the Bi spectrum can be fitted using two components as well (Fig. 3(b)): binding energies of 163.8~164.1 eV (component 1) and 163.0~163.2 eV (component 2) for the $4f_{5/2}$ peak; and 158.5~158.8 eV (component 1) and 157.7~157.9 eV (component 2) for the $4f_{7/2}$ peak. Again the binding energies being lower than for Bi^{3+} indicates the presence of oxygen deficiency.

The existence of Bi_{Ir} defects and oxygen vacancies in our pyrochlore thin films is not too surprising. First, cation antisite defects have already been observed in other pyrochlore compounds such as $\text{Gd}_2\text{Zr}_2\text{O}_7$ ⁵⁸. Second, the structure of pyrochlore $\text{Bi}_2\text{Ir}_2\text{O}_7$ is remarkably similar to that of the cubic $\delta\text{-Bi}_2\text{O}_3$ ⁵⁹ which can be viewed as $\text{Bi}_2\text{Bi}_2\text{O}_6$. Figure 4 shows a unit cell of the cubic $\delta\text{-Bi}_2\text{O}_3$, a 1/8 unit cell of $\text{Bi}_2\text{Ir}_2\text{O}_7$ with and without antisite defects and oxygen vacancies. In comparison to $\text{Bi}_2\text{Ir}_2\text{O}_7$, the cubic $\delta\text{-Bi}_2\text{O}_3$ has one less oxygen atom and all Ir sites are occupied by Bi. As a result, a significant amount of Bi_{Ir} defects and oxygen vacancies can exist in $\text{Bi}_2\text{Ir}_2\text{O}_7$ while maintaining its cubic crystal structure.

Transport measurements and discussion. With the existence of antisite defects and oxygen vacancies, the $\text{Bi}_{2+x}\text{Ir}_{2-y}\text{O}_{7-\delta}$ thin films show revealing electronic transport properties. The dependence on T of the

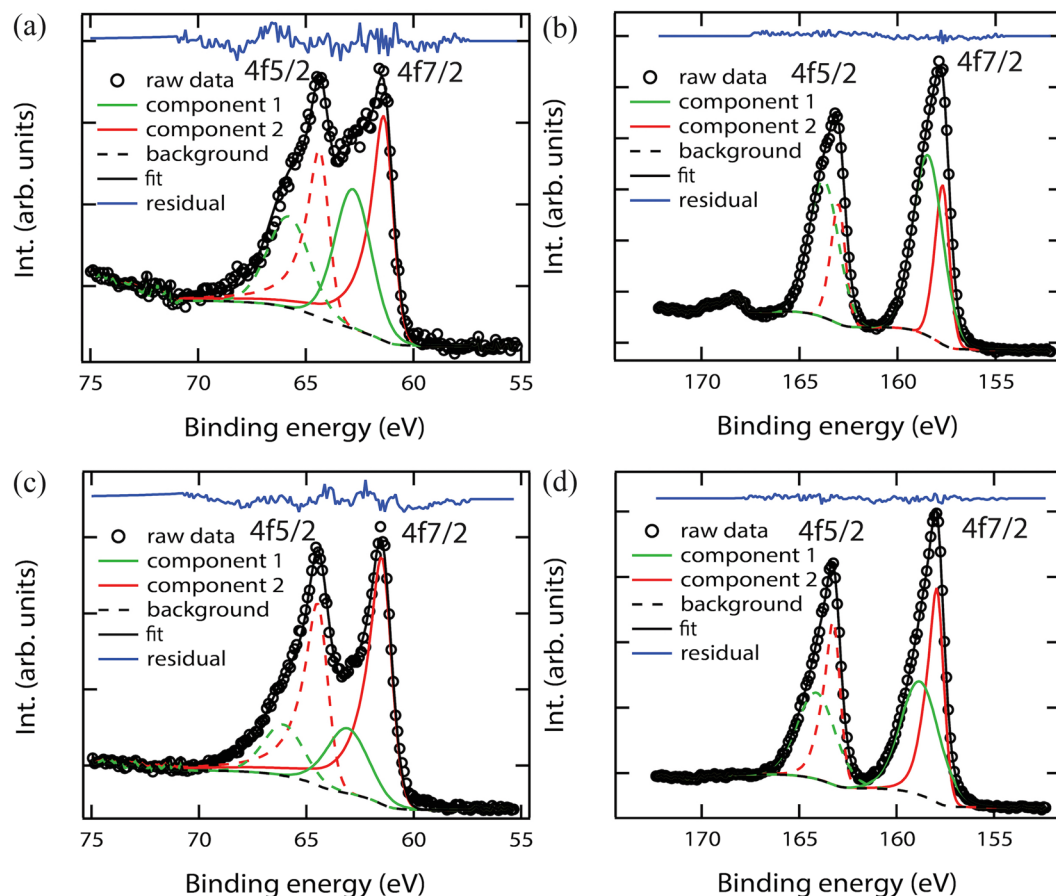


Figure 3. XPS (a) Ir $4f_{5/2}$ and $4f_{7/2}$ spectra and (b) Bi $4f_{5/2}$ and $4f_{7/2}$ spectra taken on film f1. (c) Ir $4f_{5/2}$ and $4f_{7/2}$ spectra and (d) Bi $4f_{5/2}$ and $4f_{7/2}$ spectra taken on film f3. The spectra were fitted using two components: a symmetric component (higher binding energy peak) described by the Gaussian-Lorentz profile $GL(m)$, and an asymmetric component (lower binding energy peak) by the convolution of Gelius profile $A(a,b,n)$ and Gaussian-Lorentz profile $GL(m)$. The parameters a and b are optimized as described in the supplementary information.

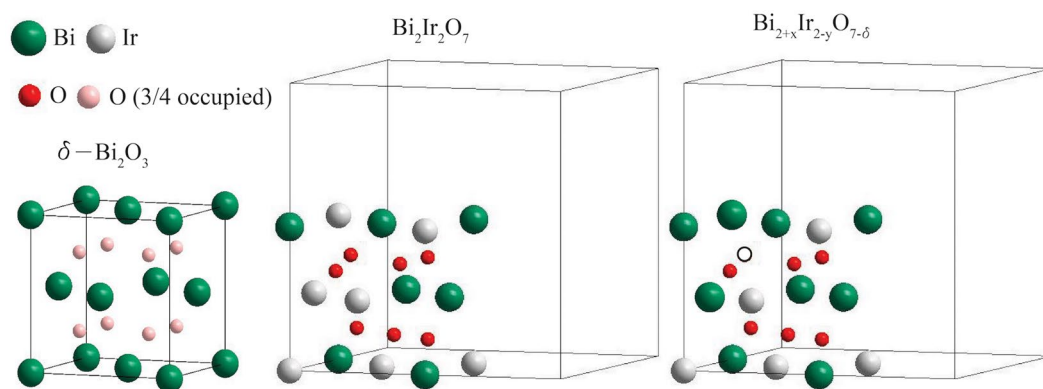


Figure 4. A unit cell of cubic δ - Bi_2O_3 , $1/8$ unit cell of $\text{Bi}_2\text{Ir}_2\text{O}_7$ and $\text{Bi}_{2+x}\text{Ir}_{2-y}\text{O}_{7-\delta}$. In the $\text{Bi}_{2+x}\text{Ir}_{2-y}\text{O}_{7-\delta}$ shown above (as an example), two Ir atoms are replaced by Bi atoms and one oxygen atom is missing (represented by the open circle).

sheet resistance (2D resistivity) R_{\square} at magnetic field $B = 0$ and the low- T magnetoresistance (MR, R_{\square} vs B) and the Hall resistance R_H vs B were obtained on Hall bars (inset in Fig. 5 and *cfr.* Methods) prepared by photolithography and dry etching on the three representative films, f1, f2, and f3. Values for R_{\square} at $B = 0$ and $T = 0.39$ K are, $483\Omega/\square$ (f1), $1334\Omega/\square$ (f2), and $1013\Omega/\square$ (f3). As observed in Fig. 5 at $T = 0.39$ K, R_H shows a non-linear

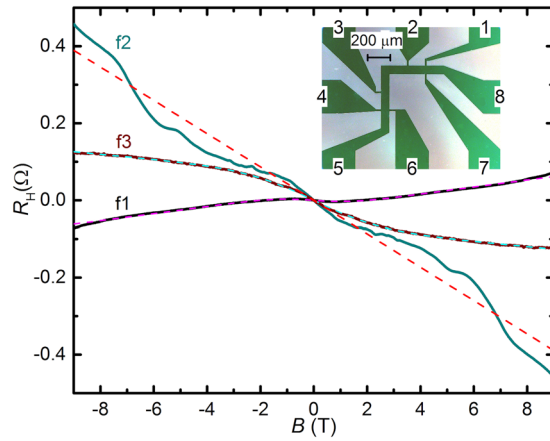


Figure 5. Hall resistance R_H vs B at $T = 0.39$ K for films f1, f2 and f3 (solid lines, films as indicated), with fits to a two-carrier model (f1, f3, dashed lines) or an averaging single-carrier model (f2, dashed line). The polarities are chosen such that a negative slope corresponds to positive charge carriers. The inset represents the L-shaped Hall bar geometry used on all 3 films (contacts 5 and 8 are current contacts, contacts 1, 2, 3, 4, 6, 7 are voltage contacts for measurement of R_H and R_{\square}).

dependence on B for all films, suggesting the existence of multiple types of charge carriers. In particular, $R_H(B)$ of f1 can be fitted to a two-carrier model by including both electrons and holes, while f3 is found to host two types of holes with different carrier mobilities. The sheet charge carrier densities (n_e for electrons, n_h for holes) and mobilities (μ_e for electrons, μ_h for holes) determined from the fittings at $T = 0.39$ K are: $n_e = 8.0 \times 10^{20} \text{ m}^{-2}$, $\mu_e = 1.5 \times 10^{-5} \text{ m}^2 \text{ V}^{-1} \text{ s}^{-1}$ and $n_h = 2.0 \times 10^{12} \text{ m}^{-2}$, $\mu_h = 0.38 \text{ m}^2 \text{ V}^{-1} \text{ s}^{-1}$ for film f1; $n_h = 6.4 \times 10^{20} \text{ m}^{-2}$, $\mu_h = 1.0 \times 10^{-5} \text{ m}^2 \text{ V}^{-1} \text{ s}^{-1}$ and $n_h = 3.0 \times 10^{12} \text{ m}^{-2}$, $\mu_h = 0.23 \text{ m}^2 \text{ V}^{-1} \text{ s}^{-1}$ for film f3. $R_H(B)$ for f2 cannot be fitted to a two-carrier model, yet the use of more than two types of carriers will lead to uncertainty in the fitting values due to the proliferation of fitting parameters. While the complicated $R_H(B)$ for f2 indicates the presence of multiple carriers, its slope indicates that the dominant charge carriers are holes, with average $n_h = 1.4 \times 10^{20} \text{ m}^{-2}$. The clear experimental evidence for the presence of multiple charge carriers in films f1, f2 and f3 is qualitatively consistent with the existence of multiple bands in the electronic structures⁶⁰. The multiple bands will impart different effective masses, qualitatively consistent also with the experimental evidence for different mobilities. While oxygen vacancies are expected to function as n -type dopants and Bi_i antisite defects as p -type dopants, it is less certain that the observed carrier densities should be associated with doping via these different types of defects since thermal ionization of defect levels may not be effective at $T = 0.39$ K. At the high defect density present in the films, e.g. where 1/3 of Ir is replaced by Bi, the defects can be expected to impact the electronic band structure instead of solely change the Fermi level via doping, not captured in DFT calculations based on assumed stoichiometry. Association between observed transport properties and specific defects therefore requires future theoretical and experimental studies of band structure in the presence of high defect densities.

All three films show metallic behavior in R_{\square} vs T at high T , as Fig. 6 shows. At intermediate T , the films show a logarithmic increase of R_{\square} with decreasing T such that $1/R_{\square} \sim \ln(T/T_0)$ (Fig. 6). The transition from metallic to logarithmic insulating behavior occurs for f1 at 10 K, for f2 at 50 K and for f3 at 55 K. It is apparent that among the three films, f1 maintains its metallic character to the lowest T , compatible with a higher crystalline quality. Indeed, XRD for f1 shows the sharpest features (see Supplementary Fig. S1), a sign of the best crystalline quality among the films. The logarithmic dependence of the sheet conductance (2D conductivity) $G_{\square} = 1/R_{\square}$ on T , depicted in Fig. 7, can at $B = 0$ be expressed as:

$$G_{\square} = G_{\square 0} + \alpha(e^2/2\pi^2\hbar) \ln(T/T_0) \quad (1)$$

where $G_{\square 0}$ denotes a T -independent part, T_0 is a normalization constant, and α denotes a prefactor. Figure 7 depicts $G_{\square}(B = 0)$ vs T on a semi-logarithmic graph, with fits to Equation (1) yielding $\alpha = 0.67$ for f1, $\alpha = 0.71$ for f2 and $\alpha = 0.87$ for f3. The values for α are typical for thin films in general, where α of order unity is most often encountered⁶¹. Two mechanisms can lead to a logarithmic dependence but in all present films have opposite effects on G_{\square} : antilocalization which will tend to increase G_{\square} with decreasing T at $B = 0$, and electron-electron interactions which will tend to decrease G_{\square} with decreasing T . Antilocalization results from the destructive interference of partial waves on time-reversed paths returning to the origin of the paths, occurring in the presence of spin-orbit interaction when the mobility mean-free-path is shorter than the quantum phase coherence length^{61–66}. Antilocalization is accompanied by a characteristic positive MR, observed in the films^{61–66}. Figure 8 shows the MR obtained at $T = 0.39$ K for the films. A pronounced low- B positive MR characteristic of antilocalization is observed for all three films, transitioning to a linear positive MR at high B (discussed below). The existence of antilocalization confirms the presence of spin-orbit interaction in the films, and accounts for the observation of relatively low $\alpha < 1$. As a quantum coherence effect, the antilocalization correction to the classical

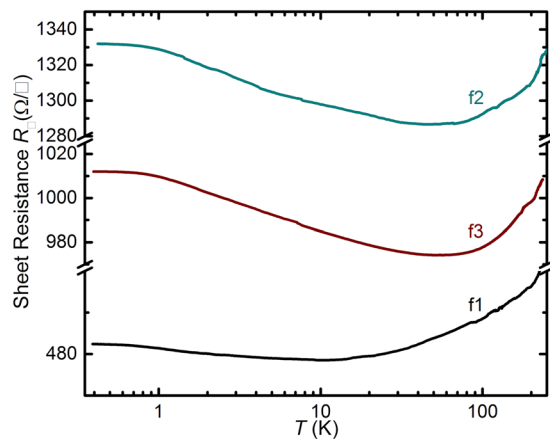


Figure 6. Sheet resistance R_{\square} vs T at $B=0$ for films f1, f2 and f3 (films as indicated).

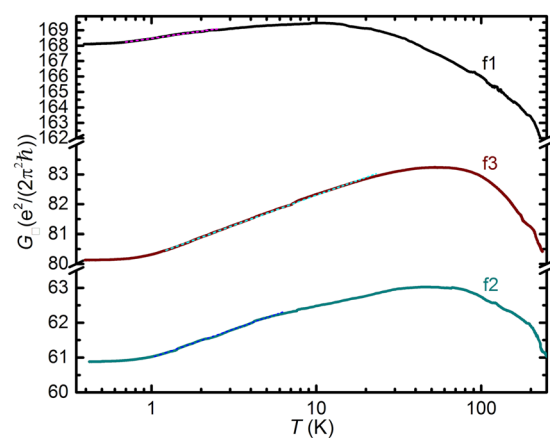


Figure 7. Sheet conductance G_{\square} vs T at $B=0$ for films f1, f2 and f3 (solid lines, films as indicated), with fits to the low- T data using Equation (1) (dashed lines).

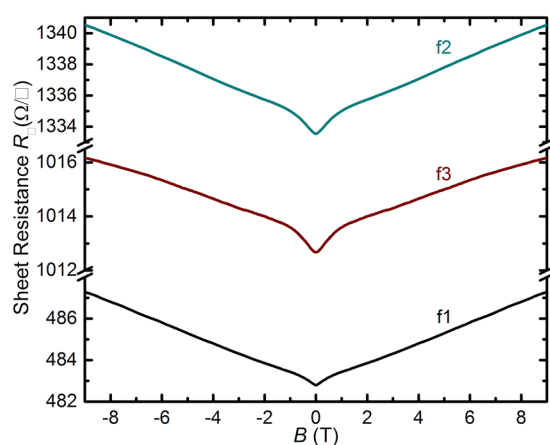


Figure 8. Sheet resistance R_{\square} vs B at $T=0.39$ K for films f1, f2 and f3 (films as indicated). A positive MR attributed to antilocalization is visible for $B < 1$ T, and a linear positive MR appears for $B > 1.5$ T.

sheet conductance strengthens with decreasing T , which increases G_{\square} with decreasing T . On the other hand, electron-electron interactions can directly decrease G_{\square} ($B=0$) with decreasing T via the Aronov-Altshuler mechanism⁶⁷, where the interaction leads to an effective suppression of the density-of-states at the Fermi level

in diffusive transport. The Aronov-Altshuler mechanism results in a logarithmic dependence on T as expressed in Equation (1) with α ranging from 0.25 (strong screening of electron-electron interactions) to 1 (no screening)^{61,66}. The Aronov-Altshuler mechanism is also accompanied by a weak positive MR⁶¹. In the present films the dependence $G_{\square} \sim \ln(T/T_0)$ down to $T \approx 1$ K with prefactor $\alpha < 1$, and the upturn in G_{\square} for $T < 1$ K are attributed to the competing effects of antilocalization and the Aronov-Altshuler electron-electron interaction mechanism. The observation of positive MR at low B (Fig. 8) is further consistent with the presence of both antilocalization and the Aronov-Altshuler mechanism. A detailed analysis of the exact contribution of each effect is outside the scope of this work. The linear positive MR at higher $B > 1.5$ T in Fig. 8 is similar to the MR observed in previous work on thin film Bi-227³⁹, although no hysteresis was observed in our thin films. We ascribe the linear positive MR at high B to the underlying electronic structure featuring a linear dispersion. Although its exact origins are still debated, a positive linear MR has indeed consistently appeared in the context of materials with a linear dispersion or quasi-relativistic dispersion (Dirac materials, topological insulators, Bi, InSb)⁶⁸.

Conclusions

In conclusion, we have achieved epitaxial growth of pyrochlore iridate thin films on yttria-stabilized zirconia substrate via pulsed laser deposition. The lattice constants of the films are a few percent larger than that of the bulk single crystal, and the film composition shows a strong dependence on the oxygen partial pressure P_{O_2} . DFT calculations indicate the existence of Bi_{Ir} , which is qualitatively consistent with the large lattice constant and low Ir/Bi ratio found in the films grown at a relatively high P_{O_2} . Both Ir and Bi have oxidation states that are lower than their nominal values, suggesting the existence of oxygen deficiency. With antisite defects and oxygen vacancies, the $Bi_{2+x}Ir_{2-y}O_{7-\delta}$ thin films show a variety of intriguing electronic transport properties, including multi-carrier transport, a logarithmic dependence of conductance on T , an antilocalization quantum correction to conductance due to spin-orbit interaction, and linear positive magnetoresistance.

Methods

Experimental details. Thin films of $Bi_{2+x}Ir_{2-y}O_{7-\delta}$ were grown on yttria-stabilized zirconia (YSZ) (111) substrates by PLD. Two ceramic targets were prepared via a solid state reaction method using IrO_2 and Bi_2O_3 as source materials at Ir/Bi ratios of 1 and 3 (labeled as Ir/Bi@1 target and Ir/Bi@3 target, respectively). The repetition rate of the KrF excimer laser ($\lambda = 248$ nm) was 1 Hz and the nominal energy density was ~ 3.33 J/cm². The substrate heater temperature was set to 750 °C (actual substrate temperature ~ 550 °C), and P_{O_2} was varied from 1 to 50 mTorr. Films grown at three representative conditions labeled as f1 ($P_{O_2} = 50$ mTorr, Ir/Bi@1 target); f2 ($P_{O_2} = 50$ mTorr, Ir/Bi@3 target); and f3 ($P_{O_2} = 15$ mTorr, Ir/Bi@3 target), were the focus of this work. After deposition, the PLD chamber was filled with oxygen gas up to about atmosphere pressure, in which thin films were cooled down. X-ray diffraction (Panalytical X'Pert PRO MRD) 2θ - ω (Triple axis mode) and φ -scans (Rocking curve mode) were carried out in Los Alamos National Laboratory to obtain information on the orientation, lattice parameters and epitaxial quality of the thin films. Further XRD measurements were also carried out in Indiana University using a standard PANalytical instrument with a Chi-Phi-Z sample stage (Cu K_{α}). Cross-section specimens for TEM were prepared by mechanical polishing of the film to a final thickness of ~ 60 μ m with a diamond lapping film, followed by a thinning process using a Gatan Precision Ion Polishing System Model 691. TEM characterization was conducted in an FEI Tecnai F30 transmission electron microscope. Energy-dispersion X-ray spectroscopy (EDX) measurement was carried out in a scanning electron microscope (SEM, Quanta FEI). X-ray photoelectron spectroscopy (XPS) data were obtained on a PHI VersaProbe II Scanning X-ray Microprobe system. All XPS spectra were calibrated using the carbon 1s peak at 284.8 eV. Magnetotransport measurements were performed on microfabricated Hall bars (*cf.* inset in Fig. 5), obtained by photolithography followed by reactive ion etching in BCl_3 . The Hall elements were L-shaped to enable characterization of anisotropic transport properties (anisotropy was not observed). The active region of the Hall elements had a length-to-width ratio of 2 (160 μ m length, 80 μ m width), sufficiently high to allow observation of a clear Hall signal despite the low values for $R_H(B)$. Ohmic contacts were photolithographically fabricated as unannealed pads of 5 nm Cr / 40 nm Au. Magnetotransport was measured over 390 mK $< T < 270$ K in a sample-in-liquid ³He system. Excitation currents varied between 5 nA (for R_{\square}) to 20 nA (for R_H), sufficiently low to avoid carrier heating. Zero-field resistances were measured during cool-down from 270 K to 390 mK with magnetic field $B = 0$ T (ZFC). Magnetoresistances were then measured at 390 mK over -9 T $< B < 9$ T. Samples were subsequently brought to $T = 30$ K and $B = 4.0$ T and cooled to $T = 390$ mK at $B = 4.0$ T (FC). Magnetoresistances were then remeasured at 390 mK over -9 T $< B < 9$ T. Differences in data between ZFC and FC conditions were not apparent and hence magnetotransport data obtained under ZFC conditions only are shown.

DFT calculation details. Density-functional theory calculations were carried out on the pyrochlore structure with and without defects by using DFT code, VASP^{69,70}. The generalized gradient approximation (GGA)⁷¹ was used for exchange-correlation functional and projector-augmented wave (PAW) pseudopotentials⁷². Spin-orbit coupling was included self-consistently within the DFT calculation. For the perfect Bi-227 pyrochlore structure, we considered a face-centered cubic (fcc) primitive unit cell of 22 atoms with the experimental lattice constant of 5.155 Å¹⁴ and relaxed the geometry until the residual forces became less than 0.01 eV/Å. The energy cutoff of 400 eV and $9 \times 9 \times 1$ k -point mesh were used for the relaxation and the self-consistent run of the optimized geometry.

For the structure with defects, we considered two different types of defects, i.e. Bi: Ir antisite (Bi_{Ir}) and Bi interstitial (Bi_{int}) that could result in the high Bi to Ir ratio found in the experiment. In each defect type, we simulated an 88-atom supercell with one defect when the structure is electrically neutral (see Supplementary Fig. S6). Possible oxygen vacancies were not introduced in the structure. In the structure with defects, the geometry was relaxed with $5 \times 5 \times 1$ k -point mesh and an energy cutoff of 400 eV until the residual forces were less than

0.01 eV/Å. The formation energy of a Bi antisite defect is $\Delta E_f = E_{anti} - E_0 - (\mu_{Bi}^{bulk} + \Delta\mu_{Bi}) + (\mu_{Ir}^{bulk} + \Delta\mu_{Ir})$, whereas the formation energy of an interstitial Bi defect is $\Delta E_f = E_{int} - E_0 - (\mu_{Bi}^{bulk} + \Delta\mu_{Bi})$, where E_{anti} , E_{int} , and E_0 are total energies of the structure with an antisite defect, with an interstitial defect, and without any defects, respectively^{73–75}. Here μ_{Bi}^{bulk} and μ_{Ir}^{bulk} are the chemical potential of bulk Bi and Ir, while $\Delta\mu_{Bi}$ and $\Delta\mu_{Ir}$ are the chemical potential differences from their bulk values. The chemical potentials of bulk Bi and Ir were calculated from DFT. The chemical potential differences depend on sample growth conditions, and their ranges are bounded by the formation enthalpy ΔH_f of Bi-227 (without defects) such as $\Delta H_f = 2\Delta\mu_{Bi} + 2\Delta\mu_{Ir} + 7\Delta\mu_O$, where $\Delta\mu_O$ is the chemical potential difference of two O atoms from an O₂ molecule in the gas phase. The DFT-calculated formation enthalpy of Bi-227 from the elemental Bi, Ir, and O₂ gas molecule is -15.08 eV. Therefore, the minimum values of $\Delta\mu_{Bi}$, $\Delta\mu_{Ir}$, and $\Delta\mu_O$ are -7.54 , -7.54 , and -2.15 eV, respectively, since their maximum values are zero. These DFT-calculated numbers assume $T = 0$. To include the temperature and oxygen pressure effect, we considered $\Delta\mu_O(T, P) = \Delta\mu_O(T, P_0) + (1/2)k_B T \ln(T/T_0)$, where the first term is the chemical potential difference of oxygen at T and pressure $P_{O_2} = 1$ atm which can be obtained by applying the ideal gas law and the standard tabulated values for the O₂ gas ($T_0 = 298$ K, $P_{O_2} = 1$ atm)⁷⁴.

References

- Kim, B. J. *et al.* Novel $J_{eff} = 1/2$ Mott state induced by relativistic spin-orbit coupling in Sr₂IrO₄. *Phys. Rev. Lett.* **101**, 076402 (2008).
- Kim, B. J. *et al.* Phase-Sensitive Observation of a Spin-Orbital Mott State in Sr₂IrO₄. *Science* **323**, 1329–1332 (2009).
- Pesin, D. & Balents, L. Mott physics and band topology in materials with strong spin-orbit interaction. *Nature Physics* **6**, 376–381 (2010).
- Yang, B. J. & Kim, Y. B. Topological insulators and metal-insulator transition in the pyrochlore iridates. *Phys. Rev. B* **82**, 085111 (2010).
- Machida, Y., Nakatsuji, S., Onoda, S., Tayama, T. & Sakakibara, T. Time-reversal symmetry breaking and spontaneous Hall effect without magnetic dipole order. *Nature* **463**, 210–213 (2010).
- Wan, X. G., Turner, A. M., Vishwanath, A. & Savrasov, S. Y. Topological semimetal and Fermi-arc surface states in the electronic structure of pyrochlore iridates. *Phys. Rev. B* **83**, 205101 (2011).
- Kim, J. *et al.* Magnetic excitation spectra of Sr₂IrO₄ probed by resonant inelastic x-ray scattering: establishing links to cuprate superconductors. *Phys. Rev. Lett.* **108**, 177003 (2012).
- Witczak-Krempa, W., Chen, G., Kim, Y. B. & Balents, L. Correlated Quantum Phenomena in the Strong Spin-Orbit Regime. *Annu. Rev. Condens. Matter Phys.* **5**, 57–82 (2014).
- Schaffer, R., Kin-Ho Lee, E., Yang, B.-J. & Kim, Y. B. Recent progress on correlated electron systems with strong spin-orbit coupling. *Rep. Prog. Phys.* **79**, 094504 (2016).
- Kargarian, M. & Fiete, G. A. Topological Crystalline Insulators in Transition Metal Oxides. *Phys. Rev. Lett.* **110**, 156403 (2013).
- Morimoto, T. & Nagaosa, N. Weyl Mott Insulator. *Scientific Reports* **6**, 19853 (2016).
- Koo, H. J., Whangbo, M. H. & Kennedy, B. J. Similarities and Differences in the Structural and Electronic Properties of Ruthenium and Iridium Pyrochlores A₂M₂O_{7-γ} (M=Ru, Ir). *J. Solid State Chem.* **136**, 269–273 (1998).
- Matsuhira, K., Wakeshima, M., Hinatsu, Y. & Takagi, S. Metal-Insulator Transitions in Pyrochlore Oxides Ln₂Ir₂O₇. *J. Phys. Soc. Jpn.* **80**, 094701 (2011).
- Qi, T. F. *et al.* Strong magnetic instability in correlated metallic Bi₂Ir₂O₇. *J. Phys. Condens. Matter* **24**, 345601 (2012).
- Yanagishima, D. & Maeno, Y. Metal-nonmetal changeover in pyrochlore iridates. *J. Phys. Soc. Jpn.* **70**, 2880–2883 (2001).
- Matsuhira, K. *et al.* Metal-Insulator Transition in Pyrochlore Iridates Ln₂Ir₂O₇ (Ln=Nd, Sm, and Eu). *J. Phys. Soc. Jpn.* **76**, 043706 (2007).
- Ishikawa, J. J., O'Farrell, E. C. T. & Nakatsuji, S. Continuous transition between antiferromagnetic insulator and paramagnetic metal in the pyrochlore iridate Eu₂Ir₂O₇. *Phys. Rev. B* **85**, 245109 (2012).
- Ueda, K. *et al.* Variation of charge dynamics in the course of metal-insulator transition for pyrochlore-type Nd₂Ir₂O₇. *Phys. Rev. Lett.* **109**, 136402 (2012).
- Disseler, S. M. *et al.* Magnetic order and the electronic ground state in the pyrochlore iridate Nd₂Ir₂O₇. *Phys. Rev. B* **85**, 174441 (2012).
- Disseler, S. M. *et al.* Magnetic order in the pyrochlore iridates A₂Ir₂O₇ (A=Y, Yb). *Phys. Rev. B* **86**, 014428 (2012).
- Tafti, F. F., Ishikawa, J. J., McCollam, A., Nakatsuji, S. & Julian, S. R. Pressure-tuned insulator to metal transition in Eu₂Ir₂O₇. *Phys. Rev. B* **85**, 205104 (2012).
- Guo, H. J. *et al.* Magnetic order in the pyrochlore iridate Nd₂Ir₂O₇ probed by muon spin relaxation. *Phys. Rev. B* **88**, 060411 (2013).
- Zhao, S. *et al.* Magnetic transition, long-range order, and moment fluctuations in the pyrochlore iridate Eu₂Ir₂O₇. *Phys. Rev. B* **83**, 180402(R) (2011).
- Sagayama, H. *et al.* Determination of long-range all-in-all-out ordering of Ir⁴⁺ moments in a pyrochlore iridate Eu₂Ir₂O₇ by resonant x-ray diffraction. *Phys. Rev. B* **87**, 100403(R) (2013).
- Shapiro, M. C. *et al.* Structure and magnetic properties of the pyrochlore iridate Y₂Ir₂O₇. *Phys. Rev. B* **85**, 214434 (2012).
- Sakata, M. *et al.* Suppression of metal-insulator transition at high pressure and pressure-induced magnetic ordering in pyrochlore oxide Nd₂Ir₂O₇. *Phys. Rev. B* **83**, 041102(R) (2011).
- Tomiyasu, K. *et al.* Emergence of Magnetic Long-range Order in Frustrated Pyrochlore Nd₂Ir₂O₇ with Metal-Insulator Transition. *J. Phys. Soc. Jpn.* **81**, 034709 (2012).
- Baker, P. J. *et al.* Weak magnetic transitions in pyrochlore Bi₂Ir₂O₇. *Phys. Rev. B* **87**, 180409(R) (2013).
- Lee, Y. S. *et al.* Infrared study of the electronic structure of the metallic pyrochlore iridate Bi₂Ir₂O₇. *Phys. Rev. B* **87**, 195143 (2013).
- Takatsu, H., Watanabe, K., Goto, K. & Kadowaki, H. Comparative study of low-temperature x-ray diffraction experiments on R₂Ir₂O₇ (R=Nd, Eu, and Pr). *Phys. Rev. B* **90**, 235110 (2014).
- Hozoi, L. *et al.* Longer-range lattice anisotropy strongly competing with spin-orbit interactions in pyrochlore iridates. *Phys. Rev. B* **89**, 115111 (2014).
- Liu, H. *et al.* Magnetic order, spin dynamics and transport properties of the pyrochlore iridate Y₂Ir₂O₇. *Solid State Commun.* **179**, 1–5 (2014).
- Zhu, W. K., Wang, M., Seradjeh, B., Yang, F. & Zhang, S. X. Enhanced weak ferromagnetism and conductivity in hole-doped pyrochlore iridate Y₂Ir₂O₇. *Phys. Rev. B* **90**, 054419 (2014).
- Ueda, K. *et al.* Magnetic Field-Induced Insulator-Semimetal Transition in a Pyrochlore Nd₂Ir₂O₇. *Phys. Rev. Lett.* **115**, 056402 (2015).
- Ma, E. Y. *et al.* Mobile metallic domain walls in an all-in-all-out magnetic insulator. *Science* **350**, 538–541 (2015).
- Tian, Z. *et al.* Field-induced quantum metal-insulator transition in the pyrochlore iridate Nd₂Ir₂O₇. *Nat Phys* **12**, 134–138 (2016).
- Sushkov, A. B. *et al.* Optical evidence for a Weyl semimetal state in pyrochlore Eu₂Ir₂O₇. *Phys. Rev. B* **92**, 241108 (2015).

38. Disseler, S. M. Direct evidence for the all-in/all-out magnetic structure in the pyrochlore iridates from muon spin relaxation. *Phys. Rev. B* **89**, 140413 (2014).
39. Chu, J.-H. *et al.* Linear magnetoresistance and time reversal symmetry breaking of pyrochlore iridates $\text{Bi}_2\text{Ir}_2\text{O}_7$. *arXiv* **1309**, 4750 (2013).
40. Fujita, T. C. *et al.* Odd-parity magnetoresistance in pyrochlore iridate thin films with broken time-reversal symmetry. *Sci Rep* **5**, 9711 (2015).
41. Fujita, T. C. *et al.* All-in-all-out magnetic domain wall conduction in a pyrochlore iridate heterointerface. *Phys. Rev. B* **93**, 064419 (2016).
42. Gallagher, J. C. *et al.* Epitaxial growth of iridate pyrochlore $\text{Nd}_2\text{Ir}_2\text{O}_7$ films. *Sci Rep* **6**, 22282 (2016).
43. Fujita, T. C. *et al.* All-in-all-out magnetic domain size in pyrochlore iridate thin films as probed by local magnetotransport. *Appl. Phys. Lett.* **108**, 022402 (2016).
44. Yang, B. J. & Nagaosa, N. Emergent topological phenomena in thin films of pyrochlore iridates. *Phys. Rev. Lett.* **112**, 246402 (2014).
45. Chen, Q., Hung, H.-H., Hu, X. & Fiete, G. A. Correlation effects in pyrochlore iridate thin films grown along the [111] direction. *Phys. Rev. B* **92**, 085145 (2015).
46. Rayan Serrao, C. *et al.* Epitaxy-distorted spin-orbit Mott insulator in Sr_2IrO_4 thin films. *Phys. Rev. B* **87**, 085121 (2013).
47. Nichols, J. *et al.* Tuning electronic structure via epitaxial strain in Sr_2IrO_4 thin films. *Appl. Phys. Lett.* **102**, 141908 (2013).
48. Chen, A. P. *et al.* Strong oxygen pressure dependence of ferroelectricity in $\text{BaTiO}_3/\text{SrRuO}_3/\text{SrTiO}_3$ epitaxial heterostructures. *J. Appl. Phys.* **114**, 124101 (2013).
49. Enriquez, E. *et al.* Oxygen vacancy-driven evolution of structural and electrical properties in $\text{SrFeO}_{3-\delta}$ thin films and a method of stabilization. *Appl. Phys. Lett.* **109**, 141906 (2016).
50. Harrell, Z. *et al.* Oxygen content tailored magnetic and electronic properties in cobaltite double perovskite thin films. *Appl. Phys. Lett.* **110**, 093102 (2017).
51. Gutiérrez-Llorente, A. *et al.* Epitaxial crystals of $\text{Bi}_2\text{Pt}_2\text{O}_7$ pyrochlore through the transformation of $\delta\text{-Bi}_2\text{O}_3$ fluorite. *APL Mater.* **3**, 036105 (2015).
52. Campagna, M., Wertheim, G. K., Shanks, H. R., Zumsteg, F. & Banks, E. Local Character of Many-Body Effects in X-Ray Photoemission from Transition-Metal Compounds: Na_xWO_3 . *Phys. Rev. Lett.* **34**, 738–741 (1975).
53. Kahl, J. M. *et al.* Understanding the Electronic Structure of IrO_2 Using Hard-X-ray Photoelectron Spectroscopy and Density-Functional Theory. *Phys. Rev. Lett.* **112**, 117601 (2014).
54. Pfeifer, V. *et al.* The electronic structure of iridium and its oxides. *Surf. Interface. Anal.* **48**, 261–273 (2016).
55. Payne, D. J. *et al.* Why is lead dioxide metallic? *Chem. Phys. Lett.* **411**, 181–185 (2005).
56. Bourlange, A. *et al.* The influence of Sn doping on the growth of In_2O_3 on Y-stabilized ZrO_2 (100) by oxygen plasma assisted molecular beam epitaxy. *J. Appl. Phys.* **106**, 013703 (2009).
57. Sanchez Casalongue, H. G. *et al.* In situ observation of surface species on iridium oxide nanoparticles during the oxygen evolution reaction. *Angewandte Chemie International Edition* **53**, 7169–7172 (2014).
58. Gregg, D. J. *et al.* Cation antisite disorder in uranium-doped gadolinium zirconate pyrochlores. *J. Nucl. Mater.* **452**, 474–478 (2014).
59. Yashima, M. & Ishimura, D. Crystal structure and disorder of the fast oxide-ion conductor cubic Bi_2O_3 . *Chem. Phys. Lett.* **378**, 395–399 (2003).
60. Wang, Q. *et al.* Experimental electronic structure of the metallic pyrochlore iridate $\text{Bi}_2\text{Ir}_2\text{O}_7$. *J. Phys.: Condens. Matter* **27**, 015502 (2014).
61. Lee, P. A. & Ramakrishnan, T. V. Disordered electronic systems. *Rev. Mod. Phys.* **57**, 287–337 (1985).
62. Akkermans, E. & Montambaux, G. *Mesoscopic physics of electrons and photons*. (Cambridge University Press, 2007).
63. Kallaher, R. L. & Heremans, J. J. Spin and phase coherence measured by antilocalization in n-InSb thin films. *Phys. Rev. B* **79**, 075322 (2009).
64. Rudolph, M. & Heremans, J. J. Spin-orbit interaction and phase coherence in lithographically defined bismuth wires. *Phys. Rev. B* **83**, 205410 (2011).
65. Hikami, S., Larkin, A. I. & Nagaoka, Y. Spin-orbit interaction and magnetoresistance in the two dimensional random system. *Prog. Theor. Phys.* **63**, 707–710 (1980).
66. Markiewicz, R. S. & Rollins, C. J. Localization and electron-interaction effects in a two-dimensional metal with strong spin-orbit scattering: Pd films. *Phys. Rev. B* **29**, 735–747 (1984).
67. Altshuler, B. L. & Aronov, A. G. Zero bias anomaly in tunnel resistance and electron-electron interaction. *Solid State Commun.* **30**, 115–117 (1979).
68. Veldhorst, M. *et al.* Magnetotransport and induced superconductivity in Bi based three-dimensional topological insulators. *physica status solidi (RRL) - Rapid Research Letters* **7**, 26–38 (2013).
69. Kresse, G. & Furthmüller, J. Efficient iterative schemes for ab initio total-energy calculations using a plane-wave basis set. *Phys. Rev. B* **54**, 11169–11186 (1996).
70. Kresse, G. & Furthmüller, J. Efficiency of ab-initio total energy calculations for metals and semiconductors using a plane-wave basis set. *Comp. Mater. Sci.* **6**, 15–50 (1996).
71. Perdew, J. P., Burke, K. & Ernzerhof, M. Generalized gradient approximation made simple. *Phys. Rev. Lett.* **77**, 3865–3868 (1996).
72. Blöchl, P. E. Projector augmented-wave method. *Phys. Rev. B* **50**, 17953–17979 (1994).
73. Zhang, S. B. & Northrup, J. E. Chemical potential dependence of defect formation energies in GaAs: Application to Ga self-diffusion. *Phys. Rev. Lett.* **67**, 2339–2342 (1991).
74. Osorio-Guillen, J., Lany, S., Barabash, S. V. & Zunger, A. Magnetism without magnetic ions: percolation, exchange, and formation energies of magnetism-promoting intrinsic defects in CaO. *Phys. Rev. Lett.* **96**, 107203 (2006).
75. Van de Walle, C. G. First-principles calculations for defects and impurities: Applications to III-nitrides. *J. Appl. Phys.* **95**, 3851 (2004).

Acknowledgements

We thank Professor J. Wang, Dr. Y. Wang, Prof. Y. Lan, Dr. C.-H. Chen and S. Cheema for fruitful discussions. S. X. Z. acknowledges start-up support from Indiana University (IU) College of Arts and Sciences. J. J. H. and Y. X. were supported for the transport measurements by the U.S. Department of Energy, Office of Basic Energy Sciences, Division of Materials Sciences and Engineering under award DOE DE-FG02-08ER46532. K.P. is grateful to John W. Villanova for creating the initial pyrochlore structure and to Denis Demchenko for an advice in computation of formation energy, and was supported by U.S. National Science Foundation DMR-1206354, San Diego Supercomputer Center (SDSC) Comet and Gordon under DMR060009N, and Advanced Research Computing at Virginia Tech. We thank the IU Nanoscale Characterization Facility for access to the scanning electron microscope. XPS instrument at Nanoscale Characterization Facility of IU Nanoscience Center was funded by NSF Award DMR MRI-1126394. The X-ray diffraction facilities at the IU Molecular Structure Center was supported by NSF Grant No. CHE-1048613. The work at Los Alamos National Laboratory was supported by

the NNSA's Laboratory Directed Research and Development Program and was performed, in part, at the Center for Integrated Nanotechnologies, an Office of Science User Facility operated for the U.S. Department of Energy (DOE) Office of Science. Los Alamos National Laboratory, an affirmative action equal opportunity employer, is operated by Los Alamos National Security, LLC, for the National Nuclear Security Administration of the U.S. Department of Energy under contract DE-AC52-06NA25396.

Author Contributions

W.C.Y., W.K.Z. and M.S. carried out thin film growth. W.C.Y. performed XRD and EDX measurements and XPS analysis. W.K.Z. carried out XRD characterizations. Y.T.X. conducted transport measurements and data analysis under the supervision of J.J.H., K.P. carried out DFT calculations and analysis. A.P.C. performed XRD characterizations under the supervision of Q.X.J., Y.L. conducted XPS measurements and guided W.C.Y. on XPS analysis. Z.L. carried out TEM characterizations and analysis under the supervision of N.L., L.H. and J.A.A. assisted on EDX characterizations. S.X.Z., J.J.H., W.K.Z., W.C.Y., and K.P. prepared the manuscript. All authors participated in discussion and reviewed the manuscript. S.X.Z. conceived and directed the overall project.

Additional Information

Supplementary information accompanies this paper at doi:[10.1038/s41598-017-06785-w](https://doi.org/10.1038/s41598-017-06785-w)

Competing Interests: The authors declare that they have no competing interests.

Publisher's note: Springer Nature remains neutral with regard to jurisdictional claims in published maps and institutional affiliations.



Open Access This article is licensed under a Creative Commons Attribution 4.0 International License, which permits use, sharing, adaptation, distribution and reproduction in any medium or format, as long as you give appropriate credit to the original author(s) and the source, provide a link to the Creative Commons license, and indicate if changes were made. The images or other third party material in this article are included in the article's Creative Commons license, unless indicated otherwise in a credit line to the material. If material is not included in the article's Creative Commons license and your intended use is not permitted by statutory regulation or exceeds the permitted use, you will need to obtain permission directly from the copyright holder. To view a copy of this license, visit <http://creativecommons.org/licenses/by/4.0/>.

© The Author(s) 2017